Istraživanjaiprojektovanja za privredu
ISSN 1451-4117
DOI:10.5937/jaes0-68238
www.engineeringscience.rs

iipp publishing

Journal of Applied Engineering Science
Original Scientific Paper,
Volume 24, Number 4, Year 2026,
no 1368, pp 741-762

THERMODYNAMIC, EXERGY AND ECONOMIC ASSESSMENT OF AN INTEGRATED RECOMPRESSION–REHEAT SUPERCRITICAL CARBON DIOXIDE BRAYTON CYCLE AND RECUPERATIVE–PREHEAT ORGANIC RANKINE CYCLE

Parmod Kumar*, Shahnawaz Alam, Kamran Rasheed

Integral University, Faculty of Engineering & Information Technology,
Department of Mechanical Engineering, Lucknow, India
**parmod@student.iul.ac.in*

A recompression-reheat (RR) supercritical carbon dioxide (sCO_2) Brayton cycle integrated with a bottoming recuperative-preheat (RP) Organic Rankine Cycle (ORC) is proposed and thermodynamically analyzed. The analysis is conducted over a turbine inlet temperature (TIT) range of 500–800 °C and compressor inlet temperature (CIT) range of 32–42 °C. Results indicate that increasing TIT improves performance, whereas increasing CIT degrades performance due to higher compression work. Increasing compressor inlet pressure improves the sCO_2 cycle performance; however, its benefit is partially offset in the integrated system due to reduced heat availability for the ORC. Higher condenser temperature and split ratio generally degrade overall system performance. Useful work increases linearly with direct normal irradiance. Exergy analysis indicates that the major irreversibilities occur in the heat exchangers due to temperature mismatches. Further, the economic evaluation provides indicative design-point economic estimates for the proposed configuration under the assumed operating conditions.

Keywords: recompression–reheat supercritical CO_2 Brayton cycle, recuperative-preheat organic Rankine cycle, thermodynamic analysis

HIGHLIGHTS

- Developed a thermodynamic model of an RR sCO_2–RP ORC cogeneration system.
- Investigated the effects of TIT, CIT, pressure levels, and split ratio.
- Exergy analysis revealed major irreversibilities in recuperative heat exchangers.
- Economic assessment indicates viable operation with 0.1437 $/kWh LCOE.

NOMENCLATURE

A	area (m²)	PTC	parabolic trough collector
ex	specific exergy (kJ/kg)	RP	recuperative-preheat
$\dot{E}_D$	exergy destruction (kW)	RR	recompression-reheat
$\dot{E}_x$	exergy rate (kW)	SPT	solar power tower
f	discount rate (%)	SR	split ratio
h	enthalpy (kJ/kg)	sCO_2	supercritical carbon dioxide
$\dot{m}$	mass flow rate (kg/s)	TEC	total expenditure cost per year ($/year)
p	pressure (kPa)	TES	thermal energy storage
$\dot{Q}$	heat transfer rate (kW)	TIC	total investment cost ($)
s	entropy (kJ/kg-K)	TIP	total incomes produced annually ($/year)
T	temperature (°C)	TIT	turbine inlet temperature (°C)
$\dot{W}$	work transfer rate (kW)	AP	aperture
CIP	compressor inlet pressure (kPa)	CON	condenser
CIT	compressor inlet temperature (°C)	i	initial state
CRF	capital recovery factor	in	inlet
CSP	concentrating solar power	int	integrated system
CT	condenser temperature (°C)	MC	main compressor

DNI	direct normal irradiance (W/m²)	ORCT	organic Rankine cycle turbine
HPT	high pressure turbine	out	outlet
HTF	heat transfer fluid	PH	primary heater
HTR	high-temperature recuperator	PUMP	pump of organic Rankine cycle
IRR	internal rate of return (%)	RC	recompressor
LCOE	levelized cost of energy ($/kWh)	RCUP	recuperator of organic Rankine cycle
LPT	low pressure turbine	RH	reheater
LTR	low temperature recuperator	SH	superheater
NPV	net present value ($)	th	thermal
ORC	organic Rankine cycle	ε	effectiveness
PBP	payback period (year)	η	

1 Introduction

Global energy demand has increased significantly over the past decade, with fossil fuels still supplying the bulk of demand despite the rapid growth of renewable technologies. According to the World Energy Outlook 2024, global hydrocarbon consumption in 2023 accounted for nearly 80% of primary energy demand and over 60% of final energy consumption. Consequently, energy-related CO_2 emissions reached a new record, underscoring the ongoing reliance on natural gas, coal, and oil in both developed and underdeveloped economies. The current policy paths suggest that overall collective CO_2emissions will reach a peak level before 2030, but the estimated decrease is not large enough to put the energy system on a track that would limit global warming to 1.5 °C. The ongoing use of fossil fuel for power production continues to pose a central hindrance to decarbonization, thus necessitating high-efficiency and less-carbon alternative energy systems that may significantly reduce the global emissions [1].

In this context, renewable energy systems have emerged as a key solution for mitigating carbon emissions while ensuring a reliable and sustainable energy supply. The current impacts of climate change including accelerated warming, extreme weather events, and extensive ecological implications, have led to international frameworks, such as the Paris Agreement, to call for rapid transitions to low-carbon production and sustainable energy systems [2]. Among sustainable options, solar energy is especially promising due to its abundance, scalability, and minimal lifecycle emissions [3]. While photovoltaic (PV) technologies convert solar radiation into electricity, CSP offers the unique capability to generate high-temperature heat, thereby facilitating electricity production through thermodynamic power cycles, and can be stored for dispatchable operation. Recent assessments show that CSP systems equipped with TES can deliver dispatchable power and support multi-output polygeneration, effectively reducing the intermittency associated with solar resources. Global deployment continues to expand, with parabolic troughs and sensible-heat storage dominating current installations despite remaining cost challenges. These trends highlight CSP's growing importance in future low-carbon energy systems and the need for continued development of advanced high-temperature, multi-cycle integration strategies [4].

Recent reviews of solar tower power plants highlight major advancements in central receiver system (CRS) technologies, including heliostats, receivers, heat-transfer fluids, and high-temperature power-cycle integration. Despite global progress, further improvements in CSP systems are needed through advanced HTFs and next-generation cycles [5]. Conventional molten-salt HTFs are limited by their thermal stability (approx. 565 °C), which restrict cycle efficiency [6]. Liquid sodium has emerged as a promising alternative due to its superior thermophysical properties and ability to operate at higher temperatures, enabling improved heat transfer and integration with high-efficiency power cycles [7–9].

Parallel to receiver development, the sCO_2 Brayton cycle has emerged as a promising power-block option due to its excellent heat-transfer characteristics near the pseudo-critical region, compact turbo-machinery, and high thermal efficiency [10]. The sCO_2power cycles have attracted considerable attention as advanced alternatives to conventional thermodynamic cycles, such as the water-based Rankine cycle and the air-based Brayton cycle. The growing demand for higher thermodynamic efficiency and the need to address limitations of traditional working fluids have accelerated interest in sCO_2systems. These cycles offer several advantages, including excellent thermal efficiencies over a heat-source temperature range of 350-800 °C, compact turbomachinery, and operational flexibility that can be used to integrate with renewable energy sources [11]. Over the last 10 years, sCO_2technology has attracted significant research interest and investment worldwide, demonstrating its potential for future-generation power systems. Previous reviews have discussed the basics of cycle layout, thermodynamic behavior, and the initial development of the test-loop for sCO_2as a safe and sustainable working fluid, with elevated temperatures that can be used to develop efficient supercritical cycles for low-grade heat recovery. Research on configurations, performance, and component issues demonstrates that sCO_2systems are typically more efficient,

smaller, and more environmentally friendly than steam and ORC cycles [12]. This cycle offers high efficiency, compact size, and wide applicability in nuclear and solar energy systems as well as in developing energy systems [13]. More current literature has extended the focus to more detailed cycle configuration analysis, modeling, and optimization strategies [14].

Among the different layouts, such as simple recuperated, partial cooling, inter-cooling, and recompression, the recompression sCO_2 Brayton cycle consistently delivers the best performance for CSP applications [15-16]. Reheating between turbine stages further increases the mean heat-addition temperature, improving specific work and off-design stability. Optimization studies show that RR layouts can achieve thermal efficiencies exceeding 50% at turbine inlet temperatures above 700 °C [17]. High recuperator effectiveness is crucial for maximizing performance and reducing cold-side exergy destruction [18]. Sarkar et al. [19, 20] conducted comprehensive thermodynamic analyses of the recompression sCO_2Brayton cycle with reheat and further optimized its performance through an extensive parametric investigation. An integrated CSP sCO_2 Brayton cycle can significantly reduce fossil-fuel dependence, achieving efficiencies near 55% and fuel savings of 10–15%, with the highest seasonal benefit occurring in summer. This hybrid approach offers a reliable, low-carbon solution for regions with high solar potential and limited fuel resources [21]. High-temperature heat sources can drive highly efficient sCO_2 cycles with strong exergo-economic potential [22]. Despite the advantages, sCO_2 cycles reject substantial medium-temperature heat (120–250 °C) in the low-temperature recuperator (LTR) and precooler.

Simultaneously, sodium retains significant enthalpy after delivering high-grade heat to the cycle. To exploit this otherwise wasted energy, ORCs are commonly used as bottoming cycles [23]. A regenerative ORC significantly enhances performance over the basic configuration, yielding up to 17.8% higher thermal efficiency, 17.6% higher exergy efficiency, and 43% lower exergy destruction. These improvements demonstrate the strong potential of ORC to efficiently recover waste heat at low to medium temperatures [24]. Thermodynamic analysis of basic and recuperator-enhanced ORCs shows that the internal heat exchanger improves efficiency and reduces component irreversibility, enabling performance recovery at lower pressure ratios to avoid turbine choking and yield higher efficiency than the basic ORC under similar conditions [25]. Among the various working fluids, toluene performs exceptionally well in the recuperative ORC model due to its higher critical temperature and dry-fluid characteristics, which promote efficient heat recovery and better thermodynamic matching. Under optimized conditions, it consistently delivers higher energy efficiency than most comparable fluids, making it a strong candidate for medium-high-temperature ORC applications [26]. Studies on advanced solar-driven systems show that coupling the sCO_2 Brayton cycle with an ORC enables efficient multi-megawatt power generation by utilizing high-temperature solar heat in the sCO_2 cycle and recovering waste heat through the ORC. Reported annual evaluations indicate electrical efficiencies of 18.33% without ORC and 19.05% with ORC, with corresponding exergy efficiencies of 23.37% and 23.63%, and payback periods of 6.37–6.51 years, demonstrating strong techno-economic feasibility [27]. Further analysis of a molten-salt-based SPT coupled with a combined sCO_2–ORC configuration has shown thermal efficiency improvements of up to 4.4%, where intercooling and ORC bottoming significantly enhance net power output relative to standard recompression cycle designs [28]. These findings demonstrate the clear thermodynamic and economic advantages of integrating ORC with sCO_2 cycles in solar-driven systems.

Recent studies have examined the nature of heat transfer, cooling approaches, and practical implementation issues of sCO_2 power cycles to solar energy systems. These articles demonstrate the potential of sCO_2 systems to enhance thermal performance, system efficiency, and reliability in the next generation of power generation [29-37]. Most studies, however, have focused on standalone cycle performance, and limited work has been done on integrated configurations that can offer effective waste heat recovery.

Although impressive progress has been made in sCO_2 Brayton cycles and ORC systems, most existing studies have focused on these systems in isolation or considered only partially integrated systems, as summarized in Table 1. Earlier studies have primarily focused on improving the thermodynamic performance of power cycles separately; while relatively little attention has been paid to utilizing high-grade and medium-grade thermal energy within integrated multi-cycle structures. Despite these developments, a comprehensive thermodynamic and techno-economic analysis of fully integrated RR sCO_2 and RP ORC systems remains limited.

Table 1. Comparative overview of previous research on sCO_2 and ORC systems, emphasizing system integration strategies and analysis scope

Ref.	Energy Source	sCO_2 Cycle	ORC	System Configuration	Analysis Type
[17]	Solar	RR	Not used	sCO_2 only	Energy + Exergy
[18]	Not specified	Recompression	Not used	sCO_2 only	Energy + Exergy + Economic
[19]	Nuclear	RR	Not used	sCO_2 only	Energy + Optimization

Ref.	Energy Source	sCO_2 Cycle	ORC	System Configuration	Analysis Type
[20]	Nuclear	Recompression	Not used	sCO_2 only	Energy + Exergy
[21]	Solar + Auxiliary Heat	RR	Not used	sCO_2 only	Energy + Exergy
[23]	Solar	Simple	Basic	sCO_2 + ORC	Energy + Exergy
[26]	Waste heat (marine)	Not used	Regenerative	ORC only	Energy + Optimization
[27]	Solar	Simple	Basic	sCO_2 + ORC	Energy + Exergy + Economic
[28]	Solar	RR	Basic	sCO_2 + ORC	Energy + Optimization
This work	Solar	RR	RP	sCO_2 + ORC	Energy + Exergy + Economic

Moreover, literature tends to focus either on system-level behavior or single-cycle behavior, and limited attention has been given to the thermodynamic behavior, exergy distribution, and performance trade-offs of fully integrated cycle designs under varying input conditions. Consequently, the overall evaluation of thermodynamic performance, exergy properties, and economic viability of cascaded RR sCO_2 Brayton and RP ORC systems remains insufficient. Therefore, a research gap exists in understanding how integrated cycles can efficiently cascade high-grade and medium-grade thermal energy to improve the system performance.

To address this research gap, the present study proposes a novel cogeneration system that integrates RR sCO_2 Brayton cycle with RP ORC. The system uses high-temperature heat source, represented through an HTF to supply thermal energy to the topping sCO_2 cycle, with the remaining waste heat recovered in the bottoming ORC. It is important to note that this work aims to assess the thermodynamic feasibility and performance of the proposed hybrid power-cycle setup, and not to perform a comprehensive engineering design of the solar power plant. Accordingly, the solar subsystem is represented through equivalent thermal boundary conditions, allowing focused analysis of the integrated power block. This approach is commonly adopted in preliminary thermodynamic investigations of advanced energy systems. In addition to thermodynamic and exergy analysis, the study incorporates a techno-economic assessment to evaluate practical feasibility.

The novelty of the present work lies in the comprehensive thermodynamic, exergy and economic evaluation of a fully integrated RR sCO_2 Brayton cycle coupled with a RP ORC, with particular emphasis on the engineering integration of these specific cycle configurations and the resulting heat-cascading pathway within the integrated power block. In the proposed configuration, high-temperature heat is utilized by the RR sCO_2 topping cycle, while the subsequent medium-temperature heat is recovered and supplied to the RP ORC, enabling further utilization of the available thermal energy. The study provides detailed insights into heat cascading, exergy distribution, component-level irreversibilities and the thermodynamic and economic performance of the integrated power block under prescribed heat-input conditions. This configuration-specific assessment contributes to the development of advanced multi-cycle integration concepts for solar-driven power systems.

The specific objectives of the present study are therefore to:

- Develop a steady-state thermodynamic model of the suggested hybrid cycle.
- Evaluate system performance with first-law and second-law analysis.
- Carry out parametric studies to investigate the effect of major operating parameters.
- Determine the design point economic estimate of the proposed setup.

Limited studies have investigated a fully cascaded RR sCO_2 and RP ORC cogeneration system, with complete thermodynamic and techno-economic characterization.

2 Materials and methods

2.1 System description

The proposed configuration consists of an RR sCO_2 Brayton cycle as the topping unit, coupled with a bottoming RP ORC. This arrangement is illustrated schematically in Fig. 1. In this study, the SPT subsystem is represented using simplified thermal input conditions for the primary heater and reheater of the sCO_2 cycle, with the focus on evaluating the thermodynamic performance of the integrated power block rather than on detailed solar field design. This approach enables focused analysis of the thermodynamic interactions between the sCO_2 Brayton cycle and the ORC subsystem. Thermal energy for the topping cycle is assumed to be supplied by a high-temperature heat source, represented through an HTF. The HTF is not explicitly modeled; instead, the solar subsystem is

represented through equivalent thermal boundary conditions to focus on the thermodynamic performance of the integrated power block rather than detailed CSP plant modeling. The sodium loop shown in Fig. 1 is treated as a thermal carrier for prescribed heat delivery, and its detailed thermodynamic state-point analysis is beyond the scope of the present study. The sCO_2 power block employs a recompression design that incorporates a main compressor and a recompressor. This split-flow design generates high- and low-temperature streams. It minimizes exergy losses and enhances overall cycle efficiency. Turbine exhaust heat is recovered by two recuperators (HTR and LTR), thereby increasing thermal efficiency. To further improve performance, the HPT and LPT are separated by a reheater. This increases the average temperature of heat addition and improves specific work output. Medium-temperature waste heat from the sCO_2 cycle, discharged via the precooler, is utilized in the ORC preheater to enhance heat recovery and generate additional power.

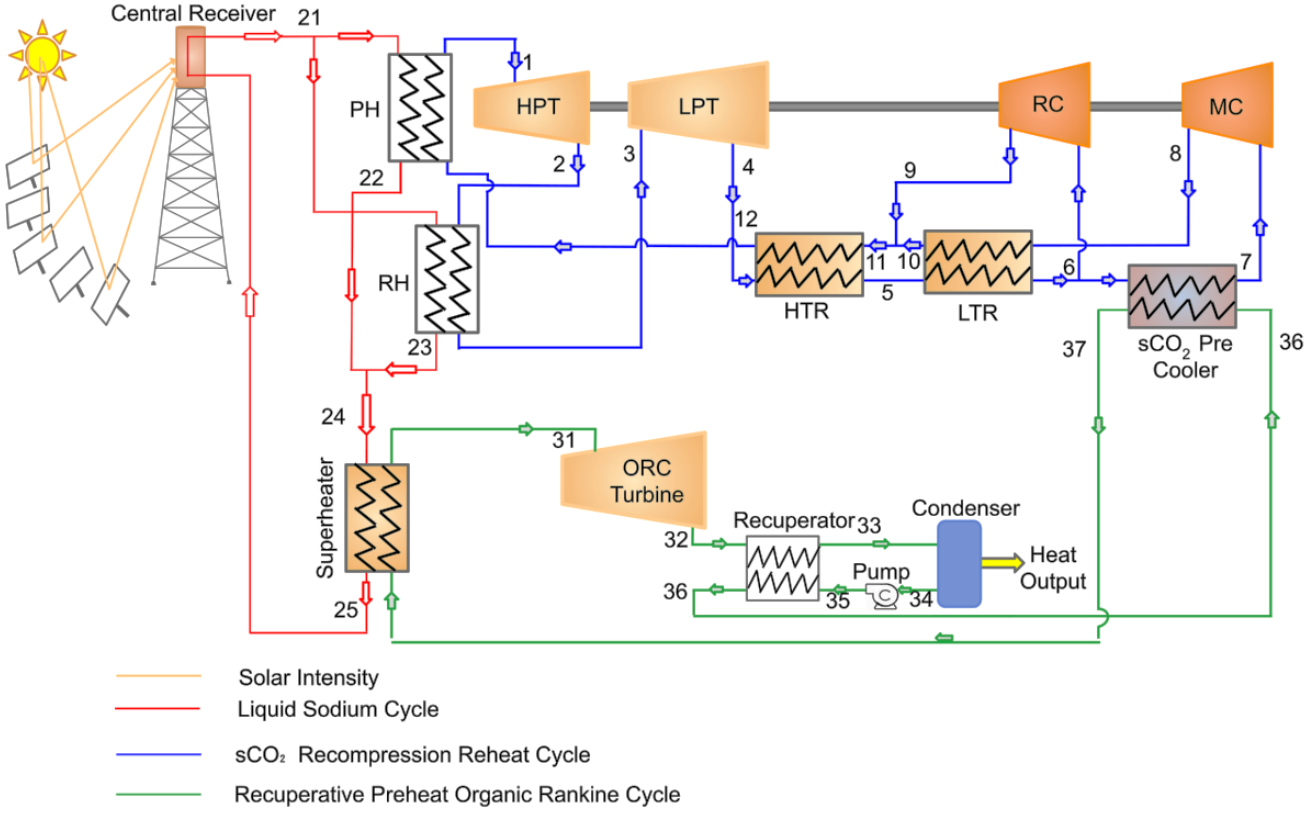

Fig. 1. Schematic diagram of a hybrid system combining RR sCO_2 Brayton cycle coupled with an RP ORC model

At high pressure, CO_2 with a critical temperature of 31.1 °C and a critical pressure of 7.38 MPa, exhibits high density and low viscosity. These properties facilitate the use of compact turbomachinery and reduce compression work. Supercritical CO_2 also exhibits superior heat transfer, enhancing recuperator performance and overall system efficiency. The CIT is selected slightly above the critical temperature of CO_2 to ensure supercritical operation. This selection enables high fluid density near the critical region, thereby reducing compression work and improving cycle performance. The selected CIT represents a reference operating condition. In practical CSP applications, particularly in arid regions with high ambient temperatures, the minimum achievable CIT is often higher. In air-cooled systems, CIT may increase to 40–45°C due to elevated ambient conditions and cooler approach temperature limitations; whereas lower temperatures may be achieved using advanced or wet cooling systems. Therefore, the present value is used to evaluate the thermodynamic potential of the cycle, while the sensitivity of system performance to CIT is addressed through parametric analysis.

The bottoming ORC employs toluene as the working fluid due to its high thermal performance, low global warming potential, and absence of ozone-depleting characteristics. Toluene's favorable thermophysical properties make it suitable for medium-temperature ORC applications in regenerative or recuperative heat-recovery processes [38-39]. For the ORC subsystem, the CT is selected based on practical cooling conditions (around 40°C), ensuring realistic heat rejection without assuming idealized low-temperature heat sinks. Accordingly, the heat rejected from the ORC condenser is available as low-grade thermal energy in the temperature range of approximately 40–50°C, which may have limited practical utilization potential depending on climatic conditions and end-user requirements.

The T–s diagrams of the RR sCO_2 Brayton cycle and RP ORC are shown in Fig. 2. TES, although widely employed in modern CSP systems to enhance dispatchability and increase capacity factor, is not included in the present study. The objective of this work is to evaluate the thermodynamic and techno-economic performance of the integrated sCO_2–ORC power block under prescribed heat-input conditions. The exclusion of TES allows isolation of the intrinsic behavior of the power-cycle configuration without additional system complexity. However, it is

acknowledged that TES plays a critical role in practical CSP operation, and its integration would significantly affect plant capacity factor and economic performance. This aspect will be considered in future work.

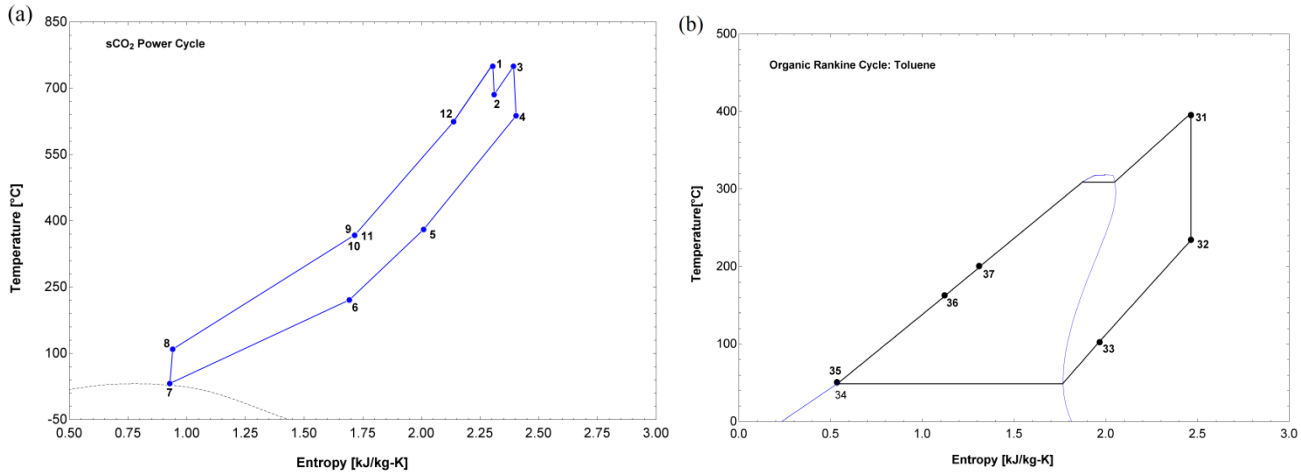

Fig. 2. T–s diagram of (a) RR sCO_2 Brayton cycle (b) RP ORC (working fluid: Toluene)

2.2 Thermodynamic modeling of the proposed system

This section presents the thermodynamic modeling framework of the proposed RR sCO_2 Brayton and RP ORC system. The solar heat input and corresponding exergy are treated as boundary conditions for the power blocks. Detailed solar-field modeling is not included in order to focus on integrated cycle performance. The HTF is treated as a constant high-temperature heat source, and its thermodynamic behavior is not explicitly evaluated in this study. The primary objective is to evaluate the thermodynamic interactions between the sCO_2 topping cycle and the ORC bottoming cycle. The analysis also considers heat cascading, overall system performance, and component-level exergy destruction. The results represent the performance trends under representative operating conditions and should be interpreted as indicative rather than exact plant-level predictions.

Thermophysical properties of the working fluids are obtained from the Engineering Equation Solver (EES) database. The behavior of sCO_2 is evaluated as a function of temperature and pressure to capture real-gas effects near the critical region. Thermophysical properties of toluene are obtained from the EES real-fluid property database as functions of both temperature and pressure to accurately model phase-change and thermodynamic processes within the ORC.

All major thermodynamic and modeling assumptions adopted in this study are summarized below for clarity and reproducibility:

- The system operates under steady-state and steady-flow conditions.
- Kinetic and potential energy effects are neglected.
- Turbines and compressors are modeled as adiabatic machines with specified isentropic efficiencies.
- Heat exchange processes are assumed to occur without any heat loss to the surroundings.
- Pressure losses are neglected, although in a practical sCO_2 system, pressure losses in heat exchangers and piping would increase compressor work, reduce turbine expansion work, alter recuperator temperature matching, and consequently reduce the predicted thermal and exergy efficiencies.
- The sCO_2 cycle operates under supercritical conditions.
- The ORC working fluid is maintained at saturation at the pump inlet.
- The solar subsystem is represented as a constant thermal heat source.
- Chemical exergy is neglected. Exergy analysis is conducted at T_o = 298.15 K and P_o = 101.3 kPa (dead state temperature and pressure, respectively).
- Mechanical and electrical losses in generators and motors are neglected, and ideal energy conversion is assumed for simplicity.

2.2.1 Energy modeling

The proposed system largely relies on component-level mass and energy balance equations. For steady-state operation, the governing equations are given as [41]:

Mass and energy conservation:

$$\sum \dot{m}_{in} = \sum \dot{m}_{out} \quad (1)$$

$$\sum \dot{Q} - \sum \dot{W} + \sum \dot{m}_{in} h_{in} - \sum \dot{m}_{out} h_{out} = 0 \quad (2)$$

where $\dot{W}$ is the work transfer rate (kW), $\dot{Q}$ is the heat transfer rate (kW), $\dot{m}$ is the mass flow rate (kg/s), and h represents the specific enthalpy (kJ/kg) at the inlet (in) and outlet (out) states of the respective components. Equations (1) and (2) are used to frame the energy balance equations for each component, as shown in Table 2.

The first-law performance is evaluated using thermal (energy) efficiency, defined as the ratio of the net work output of each power-cycle subsystem to the heat supplied. The thermal efficiencies of the sCO_2 cycle and ORC are represented by η_{th,sCO_2} and $\eta_{th,ORC}$ respectively. Both the efficiencies are calculated as follows:

$$\eta_{th,sCO_2} = \frac{\dot{W}_{HPT} + \dot{W}_{LPT} - \dot{W}_{MC} - \dot{W}_{RC}}{\dot{Q}_{PH} + \dot{Q}_{RH}} \quad (3)$$

$$\eta_{th,ORC} = \frac{\dot{W}_{ORCT} - \dot{W}_{PUMP}}{\dot{Q}_{SH} + \dot{Q}_{PC}} \quad (4)$$

The proposed integrated model produces two outputs, and the following expressions are used to compute these two outputs:

$$\dot{W}_{electricity} = \dot{W}_{HPT} + \dot{W}_{LPT} + \dot{W}_{ORCT} - \dot{W}_{MC} - \dot{W}_{RC} - \dot{W}_{PUMP} \quad (5)$$

$$\dot{Q}_{useful\ heat} = \dot{m}_{33}(h_{33} - h_{34}) \quad (6)$$

where $\dot{W}_{electricity}$ is the net power output (kW) and $\dot{Q}_{useful\ heat}$ is the recoverable low-temperature thermal energy (kW) delivered at states (33–34).

Table 2. Mass, energy and exergy formulation for the components of the proposed system

sCO_2cycle	$\dot{m}_1 = \dot{m}_2 = \dot{m}_3 = \dot{m}_4 = \dot{m}_5 = \dot{m}_6 = \dot{m}_{11} = \dot{m}_{12}$
ORC	$\dot{m}_{31} = \dot{m}_{32} = \dot{m}_{33} = \dot{m}_{34} = \dot{m}_{35} = \dot{m}_{36} = \dot{m}_{37}$
PH	$\dot{Q}_{PH} = \dot{m}_1(h_1 - h_{12})$ $\dot{E}_{x,PH} = \dot{m}_1[(h_1 - h_{12}) - T_o(s_1 - s_{12})]$
HPT	$\dot{W}_{HPT} = \dot{m}_1(h_1 - h_2) = \eta_{HPT}\dot{m}_1(h_1 - h_{2s})$
RH	$\dot{Q}_{RH} = \dot{m}_2(h_3 - h_2)$ $\dot{E}_{x,RH} = \dot{m}_2[(h_3 - h_2) - T_o(s_3 - s_2)]$
LPT	$\dot{W}_{LPT} = \dot{m}_3(h_3 - h_4) = \eta_{LPT}\dot{m}_3(h_3 - h_{4s})$
HTR	$\varepsilon_{HTR} = \frac{h_4 - h_5}{h_4 - h(t_{11}, p_5)}$ and $h_4 - h_5 = h_{12} - h_{11}$ [17]
LTR	$\varepsilon_{LTR} = \frac{h_{10} - h_8}{h(t_5, p_{10}) - h_8}$ or $\varepsilon_{LTR} = \frac{h_5 - h_6}{h_5 - h(t_8, p_6)}$ (value which have maximum heat capacity will be used) and $h_5 - h_6 = (SR)(h_{10} - h_8)$ where, split ratio (SR) is the ratio of rate of mass flow sCO_2 in main compressor to the rate of total mass flow of sCO_2 in the cycle [17]. $SR = \frac{\dot{m}_{MC}}{\dot{m}_{sCO_2}} = \frac{\dot{m}_7}{\dot{m}_6}$
MC	$\dot{W}_{MC} = SR\dot{m}_6(h_8 - h_7) = \frac{SR\dot{m}_6(h_{8s} - h_7)}{\eta_{MC}}$
RC	$\dot{W}_{RC} = (1 - SR)\dot{m}_6(h_9 - h_6) = \frac{(1 - SR)\dot{m}_6(h_{9s} - h_6)}{\eta_{RC}}$
PC	$\dot{Q}_{PC} = \varepsilon_{PC}\dot{m}_6 SR(h_6 - h_7) = \dot{m}_{37}(h_{37} - h_{36})$ $\dot{E}_{x,PC} = \dot{m}_{37}[(h_{37} - h_{36}) - T_o(s_{37} - s_{36})]$
SH	$\dot{Q}_{SH} = \dot{m}_{37}(h_{31} - h_{37})$ $\dot{E}_{x,SH} = \dot{m}_{37}[(h_{31} - h_{37}) - T_o(s_{31} - s_{37})]$
ORCT	$\dot{W}_{ORCT} = \dot{m}_{31}(h_{31} - h_{32}) = \eta_{ORCT}\dot{m}_{31}(h_{31} - h_{32s})$

RCUP	$\varepsilon_{RCUP} = \frac{h_{32} - h_{33}}{h_{32} - h(p_{33}, t_{35})}$ $(h_{32} - h_{33}) = (h_{36} - h_{35})$ [10,17]
CON	$\dot{Q}_{CON} = \dot{m}_{33}(h_{33} - h_{34}) = \dot{Q}_{useful\ heat}$
PUMP	$\dot{W}_{PUMP} = \dot{m}_{34}(h_{35} - h_{34}) = \frac{\dot{m}_{34}(h_{35s} - h_{34})}{\eta_{PUMP}}$

The overall thermal efficiency of the integrated sCO_2 and ORC power cycles ($\eta_{th,int}$) is determined by the ratio of all outputs recovered by the system to the input [40, 41].

$$\eta_{th,int} = \frac{\dot{W}_{electricity} + \dot{Q}_{useful\ heat}}{\dot{Q}_{solar}} \tag{7}$$

$$\dot{Q}_{solar} = DNI \times A_{AP} \tag{8}$$

where $\dot{Q}_{solar}$ represents the equivalent thermal input rate to the system (kW), DNI is the direct normal irradiance (W/m²), and A_{AP} is the effective aperture area of the heliostat field (m²).

2.2.2 Exergy Modeling

At constant temperature and disregarding potential and kinetic energies, the physical exergy is presented as [41]:

$$ex_i = (h_i - h_o) - T_o(s_i - s_o) \tag{9}$$

where ex represents the specific physical exergy (kJ/kg), h and s denote the specific enthalpy (kJ/kg) and entropy (kJ/kg·K), respectively, while T_o represents the ambient (dead-state) temperature.

For the case of steady state and control volume, the general equation of exergy balance is presented as [41]:

$$\sum\left(1 - \frac{T_o}{T}\right)\dot{Q} - \sum \dot{W} + \sum \dot{m}_{in}\, ex_{in} - \sum \dot{m}_{out}\, ex_{out} - \dot{E}_D = 0 \tag{10}$$

The second-law performance of the proposed hybrid system is evaluated by exergy efficiency. This is the ratio of useful exergy output to the exergy supplied to the system. The exergy efficiencies of the sCO_2 cycle, ORC cycle, and the integrated system are expressed as follows:

$$\eta_{ex,sCO_2} = \frac{\dot{W}_{HPT} + \dot{W}_{LPT} - \dot{W}_{MC} - \dot{W}_{RC}}{\dot{E}_{x,PH} + \dot{E}_{x,RH}} \tag{11}$$

$$\eta_{ex,ORC} = \frac{\dot{W}_{ORCT} - \dot{W}_{PUMP}}{\dot{E}_{x,SH} + \dot{E}_{x,PC}} \tag{12}$$

$$\eta_{ex,int} = \frac{\dot{W}_{electricity} + \dot{E}_{x,useful\ heat}}{\dot{E}_{x,solar}} \tag{13}$$

Where η_{ex,sCO_2} is the exergy efficiency of sCO_2 cycle, $\eta_{ex,ORC}$ is the exergy efficiency of ORC cycle and $\eta_{ex,int}$ is the exergy efficiency of the integrated system. Further, $\dot{E}_{x,useful\ heat}$ is the exergy of useful heat acquired by the system and has the form of [41]:

$$\dot{E}_{x,useful\ heat} = \left(1 - \frac{T_o}{T_{33}}\right)\dot{Q}_{useful\ heat} \tag{14}$$

The sun radiated exergy [41] is:

$$\dot{E}_{x,solar} = \dot{Q}_{solar}\left(1 - \frac{T_o}{T_S}\right) \tag{15}$$

where $\dot{E}_{x,solar}$ is the exergy associated with the heat source at temperature $T_s = 5777K$, which represents the effective temperature of the sun modeled as a blackbody radiation.

A systematic parametric analysis is conducted by varying one operating parameter at a time while maintaining others at baseline values (Table 3). The analysis considers key variables such as turbine inlet temperature, compressor inlet conditions, pressure levels, recompression split ratio, and solar input. The investigated parameter ranges are selected to capture representative thermodynamic behavior around the adopted design condition and near-critical sCO_2 operation. The TIT, CIT and pressure ranges encompass the operating conditions commonly investigated for sCO_2 power cycles in the cited literature, while the CT and SR ranges are selected to capture the sensitivity of the ORC bottoming cycle and heat-cascading behavior. The DNI range represents variations in solar availability rather than a site-specific annual solar resource profile. For each case, thermal efficiency, exergy

efficiency, and component-wise exergy destruction are evaluated to assess system performance trends. The present model neglects transient effects and component-level losses, which may influence actual system performance. Therefore, the present analysis represents a system-level thermodynamic assessment of the integrated power block under prescribed heat-input conditions, rather than a complete CSP plant analysis.

Table 3. Baseline values for parametric analysis and design condition

Parameters	Nomenclature	Value
Turbine inlet temperature	T_1	700 °C
Compressor inlet temperature	T_7	32 °C
Compressor inlet pressure	P_7	7,500 kPa
Turbine inlet pressure	P_1	25,000 kPa
Main and re-compressor efficiency	η_{MC} and η_{RC}	0.89
High and low pressure turbine efficiency	η_{HPT} and η_{LPT}	0.93
High & low temperature recuperator effectiveness	ε_{LTR} and ε_{HTR}	0.95
Split ratio in recompression	SR	0.62
ORC turbine efficiency	η_{ORCT}	0.75
ORC pump efficiency	η_{PUMP}	0.7
ORC recuperator effectiveness	ε_{RCUP}	0.9
Condenser temperature	T_{33}	50 °C
Heliostat field area	A_{AP}	3000 m²
Apparent sun temperature	T_s	5504 °C
Solar radiation striking on the unit area	DNI	1000 W/m²

2.3 Validation of the proposed thermodynamic model

To ensure accuracy, the proposed model is validated against previously published studies under similar boundary conditions, as summarized in Tables 4(a) and 4(b). The validation is performed at three levels: (i) the RR sCO_2 cycle, (ii) the RP ORC, and (iii) the integrated RR sCO_2– RP ORC system. The RR sCO_2 model is validated against the models of Turchi et al. [42], Foyez Ahmad et al. [21], and Kun Wang et al. [17] to establish its predictive reliability. The validation of this cycle is presented in Fig. 3, where the comparative deviations are within 4%, indicating good agreement with published results. Table 5(a) further shows relative differences of 1.45%-3.41%, further supporting the accuracy of the sCO_2 cycle model. The developed ORC model was also independently validated against reference [26] for both the recuperative configuration and the RP layout, as shown in Table 5 (b). For the recuperative configuration, the current work estimates a thermal efficiency of 35.52%, which compares with 34.15% in the reference, resulting in a deviation of 4.01%. For the recuperative and preheated setup, the calculated efficiency of 37.23% is higher than the published efficiency 35.74% by 4.16%.

The integrated system comparison with Ref. [28] shows deviations of 11.72% and 11.10%, as presented in Table 5(c).These differences should be interpreted as cross-configuration benchmark differences rather than direct measures of numerical model error, because the present study employs an RR sCO_2 cycle with an RP ORC using toluene, whereas Ref. [28] considers different sCO_2 configurations coupled with a standard ORC using isobutane. The different cycle architectures, heat-recovery arrangements, and working-fluid thermophysical properties affect heat cascading, turbine work, heat rejection, and integrated net power output. Therefore, a direct one-to-one comparison of integrated net power is not appropriate. Greater confidence in the model implementation is provided by the subsystem-level validations, where the RR sCO_2 model shows deviations of 1.45–3.41% and the ORC model shows deviations of 4.01–4.16% under comparable configurations. The integrated comparison is therefore retained as a benchmark rather than as a strict like-for-like validation.

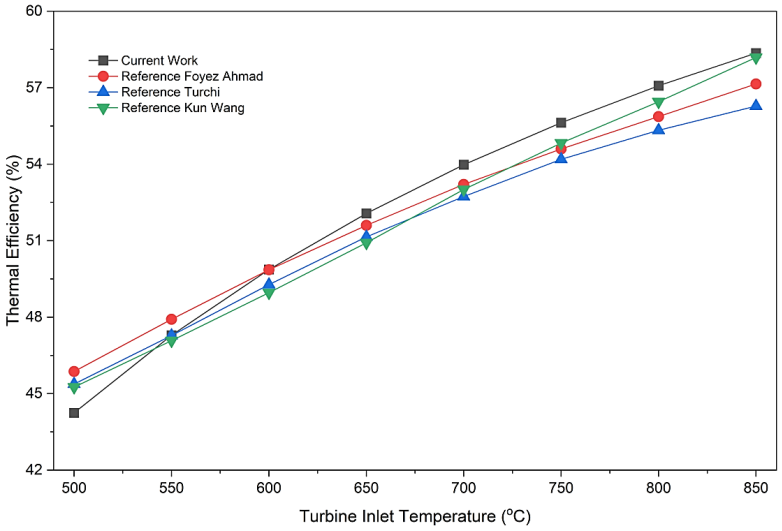

Fig. 3. Validation of the proposed RR sCO_2 model with past works [17, 21, 42]

Table 4. (a) Input data for model validation of sCO_2 as well as ORC Cycles [17, 21, 26, 42]

Parameters	Nomenclature	Value
Compressor inlet temperature	T_7	32 °C
Compressor inlet pressure	P_7	7,500 kPa
Turbine inlet temperature	T_1	500-850 °C
Turbine inlet pressure	P_1	25,000 kPa
Main and re-compressor efficiency	η_{MC} and η_{RC}	0.89
High and low pressure turbine efficiency	η_{HPT} and η_{LPT}	0.93
High and low temperature recuperator effectiveness	ε_{LTR} and ε_{HTR}	0.95
Split ratio in recompression	SR	states at outlet of LTR and recompressor are same
ORC turbine efficiency	η_{ORCT}	0.75
ORC pump efficiency	η_{PUMP}	0.7
ORC recuperator effectiveness	ε_{RCUP}	0.9
Condenser temperature	T_{33}	40 °C
Heliostat field area	A_{AP}	3000 m²
Apparent sun temperature	T_s	5504 °C
Solar radiation incident on unit area	DNI	1000 W/m²

Table 4. (b) Input data for validation of integrated $sCO_2$and ORC Cycle [28]

Parameters	Nomenclature	Value
Compressor inlet temperature	T_7	40 °C
Compressor inlet pressure	P_7	7670 kPa
Turbine inlet pressure	P_1	17200 kPa
Condenser temperature	T_{33}	40 °C
Heliostat field area	A_{AP}	10000 m²
Apparent sun temperature	T_s	5504 °C
Solar radiation striking on the unit area	DNI	800 W/m²
Ambient temperature	T_o	30 °C

Table 5. (a) Validation of the RR sCO_2 Model [based on input data from table 4 (a)]

TIT (°C)	Thermal Efficiency (%)				Relative Deviation (%)		
	Present Work	Ref. [17]	Ref. [21]	Ref. [42]	Ref. [17]	Ref. [21]	Ref. [42]
700	53.98	52.2	53.21	52.73	3.41	1.45	2.37

Table 5. (b) Validation of the RP ORC model [based on input data from table 4 (b)]

ORC Type	Thermal Efficiency (%)		Relative Deviation (%)
	Present Work	Ref. [26]	
Recuperative cycle	35.52	34.15	4.01
RP ORC	37.23	35.74	4.16

Table 5. (c) Validation of the integrated sCO_2 + ORC model [based on input data from 4(b)]

Operating Conditions	Type of Cycle	Net Power Output (kW)	Deviation (%)
TIT = 634 °C CIP = 7,670 kPa Compressor outlet pressure = 17,200 kPa	Present work: RR sCO_2+ RP ORC	2553	11.72
	Ref. [28]: Recompression sCO_2+ Standard ORC	2285	
TIT = 622 °C CIP = 7,530 kPa Compressor outlet pressure = 17,200 kPa	Present work: RR sCO_2+ RP ORC	2555.5	11.10
	Ref. [28]: sCO_2 Intercooling + Standard ORC	2300	

3 Results and discussion

The results presented in this section correspond to steady-state thermodynamic conditions and describe the performance of the proposed hybrid power cycle under representative solar heat input. The thermal input for each subsystem is defined based on its respective heat-addition boundary: (i) the sCO_2 cycle considers heat addition in the primary heater and reheater; (ii) the ORC considers heat input to the superheater from the HTF and preheating from the sCO_2 exhaust; and (iii) the integrated system efficiency is based on the total thermal energy supplied to the combined cycle. All baseline (default) values referred to in the parametric analysis correspond to the reference operating conditions listed in Table 3.

3.1 Energy and power distribution analysis

Table 6 presents the energy and power distribution of the proposed integrated system at baseline values. The total thermal input of 3000 kW represents the effective heat supplied to the power block from the solar field and receiver, modeled as an equivalent thermal input rather than explicitly separating individual solar subsystem contributions. A significant portion of the thermal input is supplied to the PH (1144 kW), the RH (584.4 kW), and the ORC superheater (459 kW) from a representative thermal input of 3000 kW supplied to the power block. The LPT (965.6 kW) produces the highest power, followed by the HPT (566.7 kW) and the ORC turbine (322.6 kW). The higher LPT output is due to reheating, which increases the inlet temperature and causes a larger enthalpy drop during low-pressure expansion. This behavior is consistent with reheated Brayton cycle behavior, where reheating increases the average expansion temperature and enhances turbine work output. The RC consumes more power (388.2 kW) than the MC (205.2 kW) due to the higher inlet temperature and lower fluid density. The ORC pump requires little power (8.225 kW). Overall, the results show favorable thermodynamic energy utilization, with the LPT making a strong contribution to power output and significant energy used in the recompression cycle, which is characteristic of RR sCO_2 Brayton cycles. A portion of the energy is recovered as useful heat (127.1 kW), which supports cogeneration. The thermal input that is not converted into useful work or useful heat is mainly lost due to exergy destruction in system components. The exergy destruction analysis in the next section provides more details on this.

Table 6. Energy and power distribution of the proposed integrated system at baseline conditions

Category	Component	Value (kW)
Heat Input	Representative thermal input to power block	3000
	Primary Heater	1144
	Reheater	584.4
	ORC Superheater	459
Power Output	HPT	566.7
	LPT	965.6
	ORC Turbine	322.6
Useful Heat Output	Recovered useful heat	127.1
Power Consumption	Main Compressor	205.2
	Recompressor	388.2
	ORC Pump	8.225

3.2 Component-wise exergy destruction analysis

The distribution of exergy destruction across system components provides insight into the dominant sources of thermodynamic irreversibility in the proposed integrated cycle, as illustrated in Fig. 4.

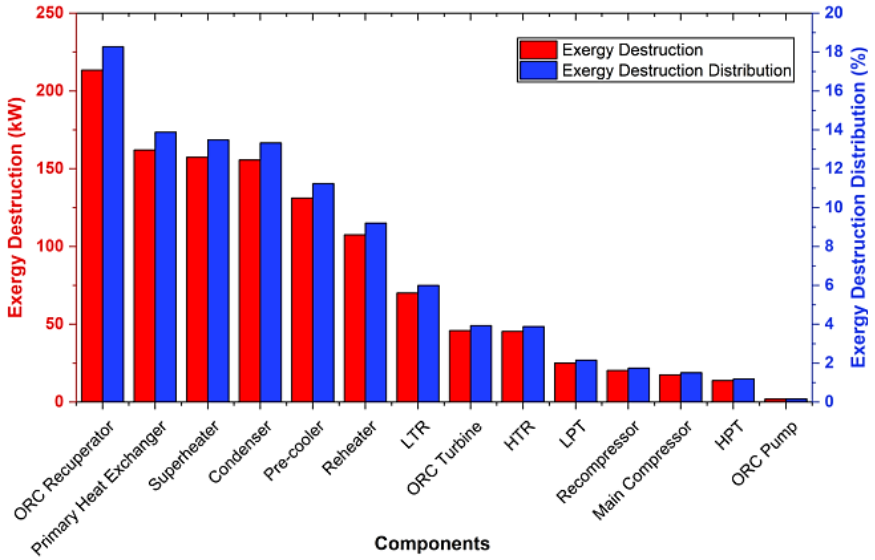

Fig. 4. Exergy destruction and its distribution in significant units of the RR sCO_2 cycle coupled with the RP ORC

The results indicate that the PH and recuperative heat exchangers contribute the most to system irreversibilities. This observation aligns with previous studies, which identify heat exchangers as the primary contributors to exergy destruction due to temperature mismatch during heat transfer. The dominant irreversibility in these components is primarily associated with heat transfer across finite temperature differences between the hot and cold streams, leading to significant entropy generation. In the PH, high-temperature heat from HTF is transferred to the sCO_2 working fluid over a broad temperature range. The temperature profiles of the two streams cannot remain identical throughout the heat exchanger because of differences in their inlet temperatures and heat capacities. Consequently, finite temperature differences persist along the heat-transfer path; particularly where the temperature driving force is relatively large, resulting in significant entropy generation and exergy destruction. Furthermore, the transfer of high-temperature heat to the sCO_2 stream involves degradation of high-grade thermal energy, making the PH a major source of irreversibility.

Similarly, the recuperators, including the HTR, LTR, and ORC recuperators, facilitate internal heat exchange between streams with different temperatures and heat capacities. Although recuperation reduces the external heat requirement, the hot and cold streams cannot achieve complete thermal matching under finite heat-transfer conditions. The resulting temperature mismatch produces entropy generation during heat recovery. The magnitude of exergy destruction is also influenced by the substantial heat duty handled by these components; therefore, even moderate temperature differences can result in considerable exergy destruction. In contrast, the lower exergy destruction associated with turbomachinery components indicates that, under the adopted component efficiencies

and steady-state assumptions, heat-transfer irreversibilities constitute the dominant thermodynamic penalty in the system. From an engineering perspective, the exergy destruction of these heat exchangers can be reduced by improving temperature matching between the hot and cold streams, increasing effective heat-transfer area and optimizing the exchanger configuration. However, increasing heat-transfer area and effectiveness may increase capital cost and pressure losses. Therefore, practical heat-exchanger design requires a trade-off among thermal effectiveness, heat-transfer area, pressure drop, and economic cost. Since the present study is focused on system-level thermodynamic characterization, detailed pinch-point and heat-exchanger sizing optimization is beyond its scope.

3.3 Parametric analysis

3.3.1 Effect of turbine inlet temperature

Figure 5 (a) and (b) present the effect of the TIT of HPT on the thermal and exergy efficiencies of RR sCO_2 cycle, RP ORC cycle, and the integrated sCO_2-ORC system, while all other parameters are held at baseline values. Over the investigated TIT range (500 °C to 800 °C), both thermal and exergy efficiencies of the sCO_2 cycle increase steadily. This trend is consistent with previously reported sCO_2 cycle behavior, where higher TIT improves efficiency by increasing the average temperature of heat addition, leading to enhanced thermodynamic performance and higher specific turbine work. In contrast, the ORC exhibits a slight decrease in thermal efficiency, as a larger fraction of high-grade heat is utilized in the sCO_2 topping cycle, thereby reducing the heat supplied to the bottoming cycle. However, the ORC's exergy efficiency increases marginally, as waste heat at higher TIT has improved thermodynamic quality, enabling more effective exergy recovery. For the integrated system, both thermal and exergy efficiencies increase across the investigated TIT range, indicating that the performance improvements in the sCO_2 cycle outweigh the minor reduction in ORC thermal efficiency. This behavior reflects a trade-off between energy utilization in the topping and bottoming cycles, with enhanced sCO_2 performance dominating overall system efficiency.

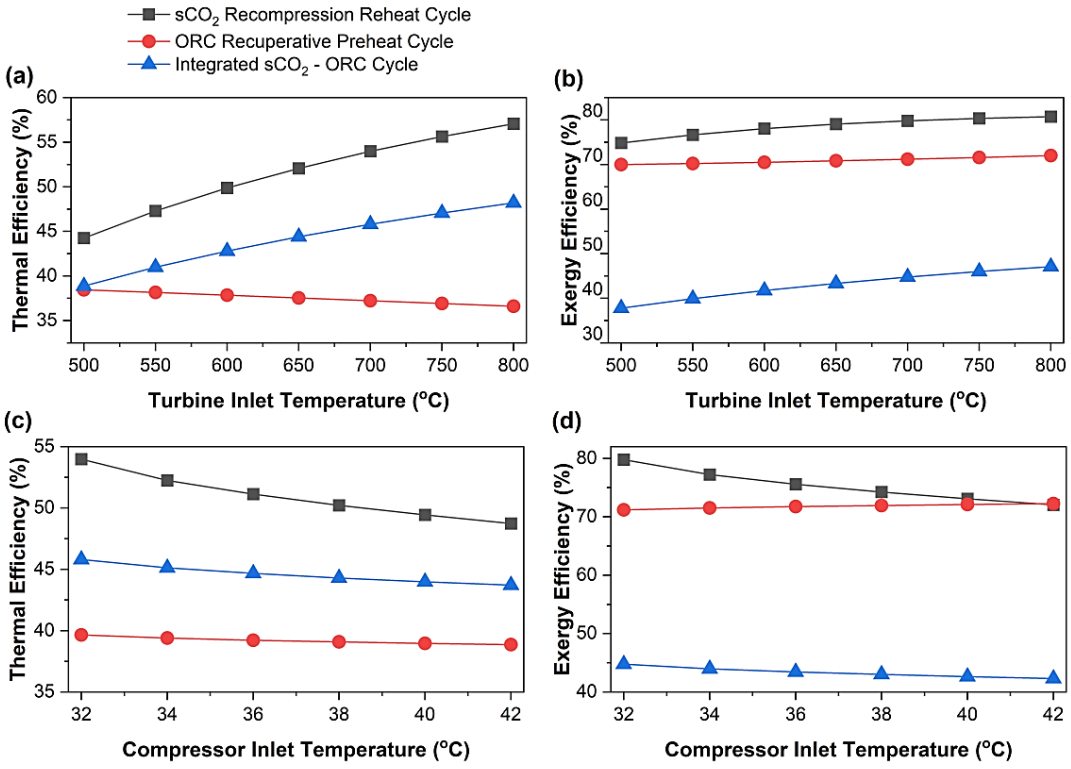

Fig. 5. Variation of thermal and exergy efficiencies with (a, b) TIT and (c, d) CIT for the RR sCO_2 cycle, RP ORC cycle, and integrated system

3.3.2 Effect of compressor inlet temperature

Figures 5(c) and 5(d) show the effect of CIT on system performance as it increases from 32 °C to 42 °C, with all other parameters kept at their baseline values. The sCO_2 cycle exhibits notable sensitivity to CIT. As CIT increases, thermal efficiency decreases from 53.98% to 48.74%, and exergy efficiency declines from 79.79% to 72.04%. This reduction is primarily due to the decrease in CO_2 density near the critical region as CIT rises, which increases the specific compression work and reduces the net cycle output. This behavior is consistent with earlier studies, particularly near the critical region of sCO_2, where fluid properties strongly influence compression work. Additionally, a higher CIT makes temperature matching in the recuperator more difficult, thereby reducing internal heat recovery and increasing exergy destruction. In contrast, the ORC shows a slight decrease in thermal efficiency from 39.66%

to 38.86%, while its exergy efficiency increases slightly from 71.18% to 72.25%. This occurs because the exhaust heat from the sCO_2 cycle is available at a higher temperature, improving its thermodynamic quality and enabling more effective exergy utilization, despite a slight reduction in heat quantity. For the integrated system, both thermal and exergy efficiencies decrease steadily with increasing CIT, dropping from 45.81% to 43.71% and from 44.76% to 42.32%, respectively. This trend is mainly due to increased compressor work at higher inlet temperatures, resulting in reduced net work output. These results demonstrate that CIT is a critical parameter influencing the thermodynamic performance of the overall system. This also reflects practical CSP operation, where higher ambient temperatures can shift the CIT toward higher values, affecting overall system performance.

3.3.3 *Effect of compressor inlet pressure*

Figures 6(a) and 6(b) show the effects of CIP on the thermal and exergy efficiencies of the RR sCO_2 cycle, the RP ORC, and the integrated system, while keeping all other parameters at baseline values. As CIP increases from 7300 kPa to 8000 kPa, the sCO_2 cycle shows improved performance, with both thermal and exergy efficiencies increasing due to a reduced compression ratio and higher CO_2 density, which lowers specific compression work. This behavior is consistent with reported sCO_2 cycle trends, where operation at higher pressures near the critical region improves compression characteristics and cycle performance. In comparison, the ORC shows a slight increase in thermal efficiency but a marginal decrease in exergy efficiency, because a larger fraction of high-grade thermal energy is utilized in the sCO_2 cycle, reducing the heat available for ORC. For the integrated system, both thermal and exergy efficiencies decrease slightly, indicating that the improvement in the sCO_2 cycle is partially offset by reduced performance of the ORC subsystem.

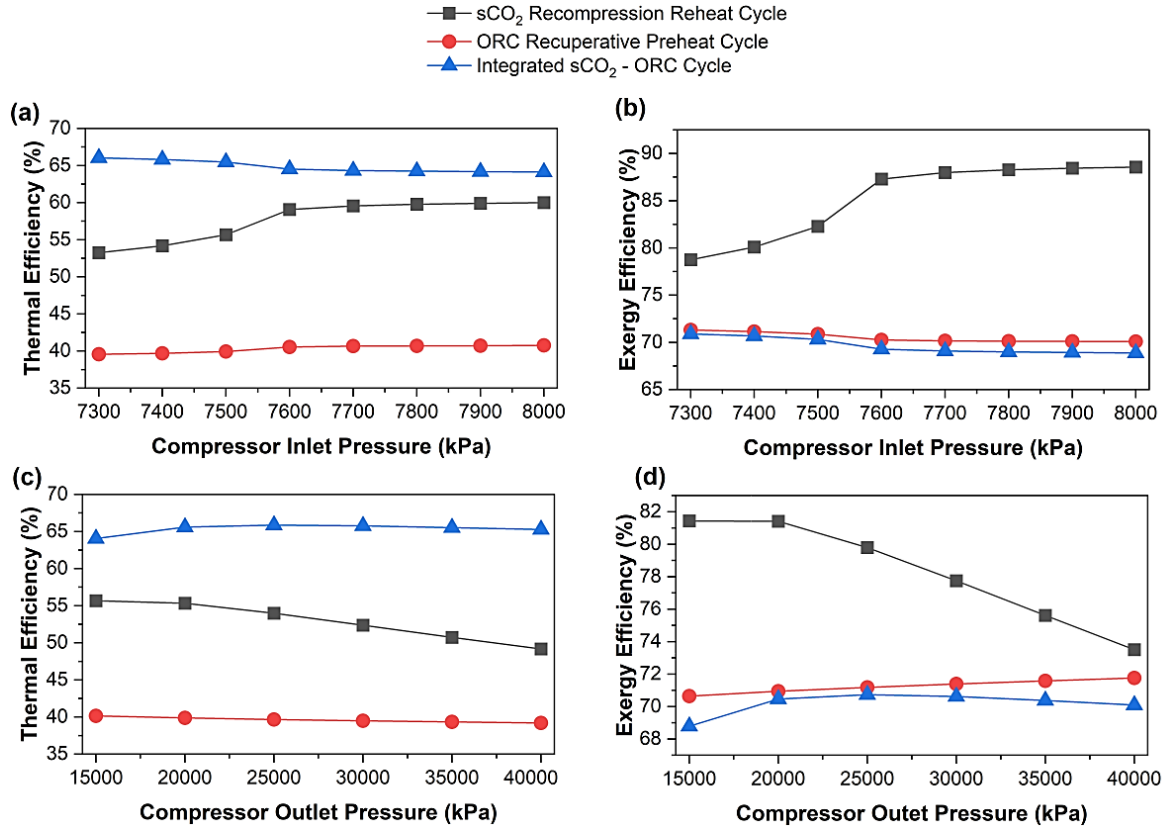

Fig. 6. Variation of thermal and exergy efficiencies with (a, b) CIP and (c, d) compressor outlet pressure for the RR sCO_2 cycle, RP ORC cycle, and integrated system

3.3.4 *Effect of compressor outlet pressure*

The effect of compressor outlet pressure variation from 15000 kPa to 40000 kPa is illustrated in Figs. 6 (c) and 6 (d), with all other parameters fixed at their baseline values. As the outlet pressure rises, the sCO_2 cycle shows a pronounced decline in performance, with thermal efficiency decreasing from 55.67% to 49.17% and exergy efficiency from 81.44% to 73.50%. This is mainly because an increased pressure ratio leads to high specific compression work and reduces net work output, hence decreasing thermal efficiency. Furthermore, higher outlet pressure adversely affects temperature matching in the recuperators, reducing internal heat recovery and increasing exergy destruction. In contrast, there is a slight decline in the ORC thermal efficiency (40.16% to 39.21%) while exergy efficiency rises moderately (70.64% to 71.76%). This occurs because higher outlet pressures result in higher waste-heat temperatures, thereby improving its thermodynamic quality and enabling more effective energy utilization, despite a slight reduction in total heat input. Consequently, both the thermal and exergy efficiencies of the integrated system decrease slightly with increasing compressor outlet pressure. This indicates

that the adverse effect of increased compression work in the sCO_2 cycle outweighs the marginal improvement in ORC performance due to higher-temperature waste heat.

3.3.5 Effect of condenser temperature

Figure 7 (a) and (b) depict the variation in first and second law efficiencies resulting from varying the CT by keeping other parameters at their baseline. As the CT increases up to 60 °C, the sCO_2 cycle shows negligible variation in both thermal and exergy efficiencies (53.98% and 79.79%, respectively). This behavior is expected, as heat rejection in the sCO_2 cycle occurs through a dedicated precooler, which is thermodynamically decoupled from the ORC condenser conditions. However, in the ORC cycle, the thermal efficiency declines steadily from 42.99% to 38.08%, and exergy efficiency declines from 81.87% to 66.26%. This decline is attributed to higher condensation temperatures, which increase condensation pressure, reduce turbine expansion ratio, and enhance entropy generation during heat rejection. Further, both the efficiencies of the integrated plant are reduced prominently to 67.67% and 72.67%, respectively, as the CT increases. The major cause of such decreases lies in the decline in the ORC performance, while the stability of the sCO_2 cycle opposes the overall sensitivity. These results indicate that CT is a critical parameter governing the bottoming cycle's performance and significantly influencing the overall system efficiency.

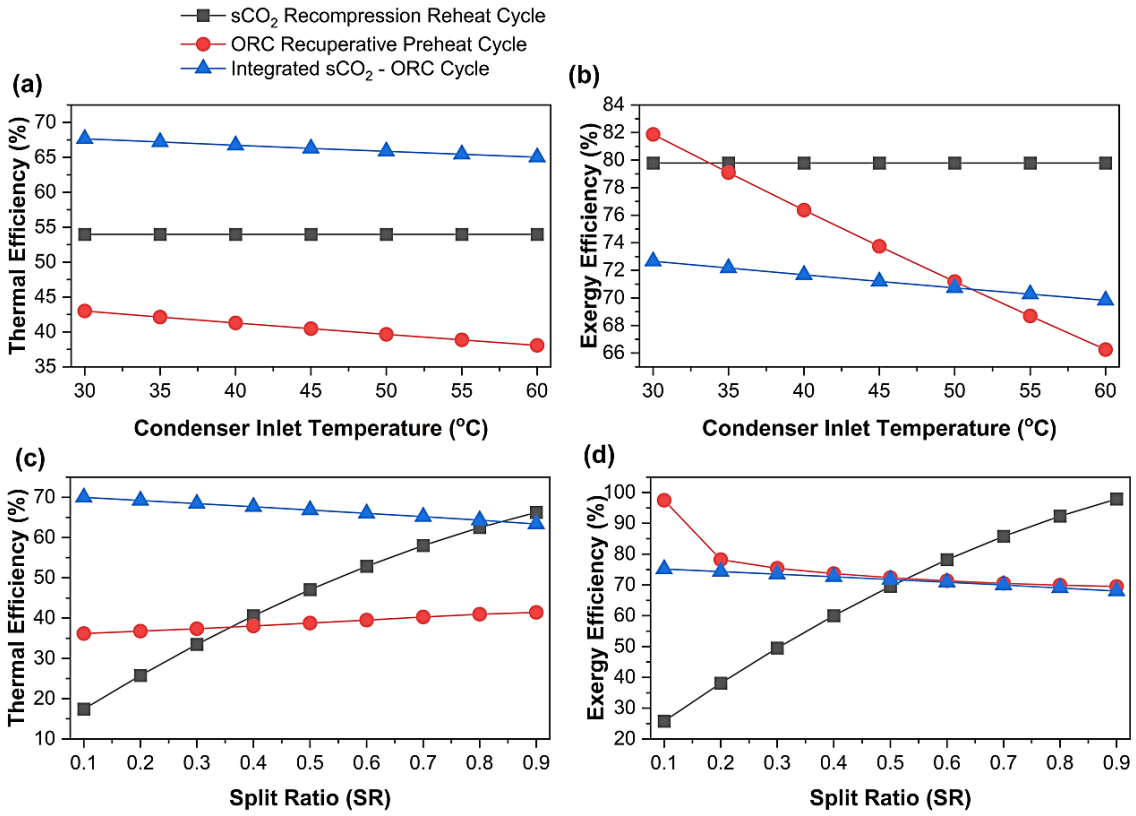

Fig. 7. Variation of thermal and exergy efficiencies with (a, b) CT and (c, d) SR for the RR sCO_2 cycle, RP ORC cycle, and integrated system

3.3.6 Effect of split ratio

Figure 7(c) and (d) illustrate the effect of SR on system efficiency. As SR increases from 0.1 to 0.9, both thermal and exergy efficiencies of the sCO_2 cycle increase significantly from 17.43% to 66.22%, and from 25.77% to 97.88%, respectively. This enhancement results from improved heat recuperation in the LTR, where increased mass flow through the main compressor improves temperature matching and reduces irreversibilities. Under the adopted idealized boundary conditions, the sCO_2 topping cycle approaches a high internal heat-recovery limit, resulting in a calculated exergy efficiency of 97.88%. It should be noted that this high exergy efficiency represents the RR sCO_2 topping cycle only. It is calculated using the exergy-efficiency formulation defined earlier, in which the denominator represents the increase in physical flow exergy of the sCO_2 working fluid across the primary heater and reheater. The relatively high value is associated with the cycle-level boundary and the idealized steady-state design-point assumptions adopted in the present model, including negligible pressure losses, high recuperator effectiveness, and absence of mechanical/electrical losses. Hence, the 97.88% value is considered an idealized upper-limit result for the RR sCO_2 topping cycle under the prescribed assumptions. In the ORC, thermal efficiency increases moderately from 36.2% to 41.42%. This behavior is associated with increased heat rejection from the sCO_2 cycle, which raises the available heat input to the ORC. Conversely, exergy efficiency declines markedly from 97.51% to 69.52% because the heat supplied to the ORC at higher SR possesses lower thermodynamic quality,

indicated by a lower average temperature. This leads to higher entropy generation and reduced exergy utilization. For the integrated system, both thermal and exergy efficiencies decrease consistently with increasing SR, declining from 69.98% to 63.35% and from 75.15% to 68.03%, respectively. This trend reflects a trade-off between improved performance of the sCO_2 cycle and reduced ORC contribution due to diminished availability of high-grade heat. Overall, the split ratio serves as a critical design parameter that determines the balance between internal heat recuperation and effective waste heat utilization in an integrated system.

3.3.7 Effect of DNI

Figure 8 shows the variation of useful work and exergy efficiency with DNI at various TIT. The variation of DNI represents different solar availability conditions rather than site-specific data. Useful work increases linearly with DNI for all TIT values, reflecting the corresponding rise in thermal energy input. Higher TIT values yield greater power output, as indicated by the upward shift of the curves, although DNI remains the primary influencing factor. Exergy efficiency exhibits a non-monotonic behavior at lower TIT values (up to 700 °C), where it increases slightly at low DNI (500–650 W/m²) and then decreases beyond approximately 650–700 W/m². In contrast, at higher TIT values (≥ 750 °C), exergy efficiency decreases monotonically with increasing DNI. This behavior is attributed to increased irreversibilities at higher heat input levels, where larger temperature differences and higher heat flux lead to greater entropy generation. Although higher TIT improves exergy efficiency across all DNI values, it does not alter the overall decreasing trend at elevated DNI. In summary, useful work rises with DNI, while exergy efficiency peaks at moderate irradiance, highlighting a trade-off between energy input and thermodynamic performance.

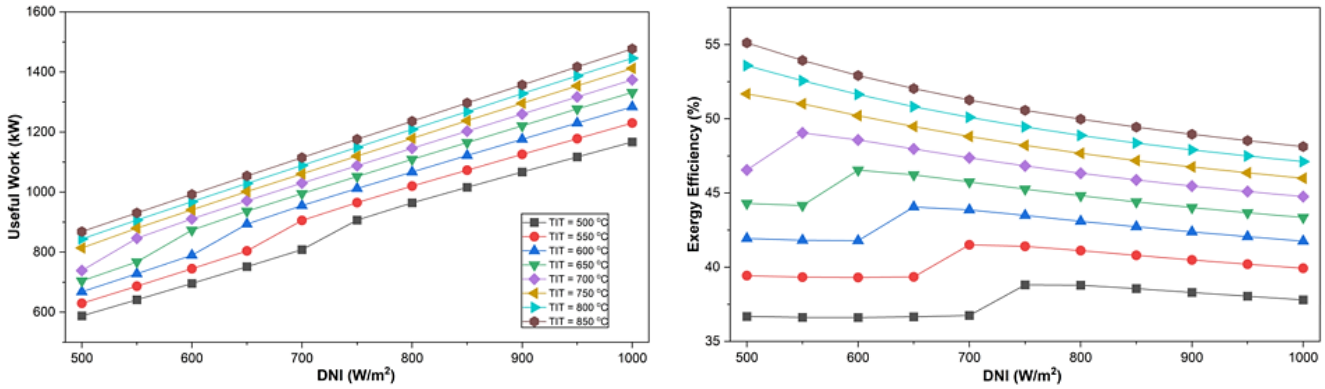

Fig. 8. Variation of exergy efficiencies and useful work with DNI for the integrated system

The present study does not employ a formal multi-objective optimization algorithm; however, the parametric results provide an indication of a favorable operating region for the proposed integrated system. Within the investigated range, higher TIT generally improves the thermal and exergy performance of the integrated system, whereas lower CIT favors performance by reducing compression work. The integrated-system performance also deteriorates with increasing compressor outlet pressure, while lower condenser temperature generally benefits the ORC bottoming cycle. Similarly, higher DNI increases useful work but do not necessarily maximize exergy efficiency. Accordingly, the present parametric results suggest that high TIT, low CIT, moderate pressure levels and low-to-moderate condenser temperature constitute a favorable operating region, subject to practical component and heat-transfer constraints. A formal multi-objective optimization considering thermal efficiency, exergy efficiency, net power output, and economic indicators would be required to determine a global optimum and is identified as an important direction for future work.

3.4 Economic analysis

An economic analysis is carried out to assess the economic feasibility of the proposed system at the design point, based on operating conditions listed in Table 3, with the TIT fixed at 800 °C. The key economic assumptions are summarized in Table 7(a).

Electricity and heat prices are assumed to be 0.232 $/kWh and 0.116 $/kWh, respectively, adopted from [41] and adjusted for inflation. These values are intended to represent high-value energy scenarios, such as industrial applications or peak-demand conditions, and may vary depending on region and market context. The recovered thermal energy at a condenser temperature of 50 °C is classified as low-grade heat and is assumed to be utilized in low temperature applications such as space heating and domestic hot water.

An equivalent annual operating duration of 8000 h/year is adopted only as a reference condition for comparative design-point economic assessment. This value is not intended to represent the actual annual solar operating duration or capacity factor of a standalone CSP plant without TES. Accordingly, the resulting economic indicators represent indicative economic potential under the prescribed operating-duration assumption rather than plant-level annual economic forecasts.

The evaluation includes TIC, TEC, and TIP, based on cost correlations available in the literature [41, 43–44, 47] and represented in Tables 7 (b, c and d). The analysis is performed using subsystem-level cost correlations

expressed in $/kW, as obtained from the literature [47]. In this approach, major system units such as the solar field, receiver, tower, and power blocks are treated as aggregated subsystems rather than being decomposed into individual components.

Table 7. (a) The assumptions taken in economic analysis

Discount rate	10 %
Plant life time	20 years
Annual operating hours [41]	8000 h/year
Cost of electricity produced [41]	0.232 $/kWh
Cost of heat produced [41]	0.116 $/kWh

Table 7. (b) The investment cost of the proposed system [47]

Unit	Installed Cost ($/kW)	Total Cost ($)
Heliostat Field	1768	2, 360,280
Receiver	876	1,169,460
Tower	130	173,550
Power Blocks	993	1,325,655
BoP & Engineering, etc.	1086	1,449,810
Contingencies	878	1,172,130
Total Investment Cost (TIC)	5,731	7,650,885

Table 7. (c) Expenditure of the proposed system/year [43-44]

Expenditure	$/year
Operation & Maintenance cost (5% of TIC)	382,544
Personal cost	100,000
Insurance cost (2% of total investment cost)	153,018
Total Expenditure Cost per Year (TEC)	635,562

Table 7. (d) Income produced from proposed system/year [41]

Income	$/year
Income Produced from Electricity (1335 kW x 8000 h/year x 0.232 $/kWh)	2,477,760
Income Produced from Heating (141.6 kW x 8000 h/year x 0.116 $/kWh)	131,405
Total Income Produced per Year (TIP)	2,609,165

Financial indicators such as PBP, NPV, CRF, LCOE, and IRR are calculated. The total investment cost corresponds to a plant capacity of approximately 1.33 MW, based on the net power output of the integrated system.

The total income from operation (TIO) is determined as [41]:

$$\mathrm{TIO} = \mathrm{TIP}\text{-}\mathrm{TEC} \tag{16}$$

The PBP is evaluated using the logarithmic expression noted in Ref. [43]:

$$\mathrm{PBP} = \frac{\ln\left(\frac{\mathrm{TIO}}{\mathrm{TIO}-\mathrm{TIC}\times \mathrm{f}}\right)}{\ln(1+\mathrm{f})} \tag{17}$$

Evaluation of the NPV of the system after Ref. [43] can be represented as:

$$\mathrm{NPV} = \mathrm{TIO}\left(\frac{(1+\mathrm{f})^{\mathrm{N}}-1}{\mathrm{f}(1+\mathrm{f})^{\mathrm{N}}}\right) - \mathrm{TIC} \tag{18}$$

The mathematical equations of CRF and LCOE are stated below [45-46].

$$CRF = \frac{f(1+f)^N}{(1+f)^N - 1} \quad (19)$$

$$LCOE = \frac{TIC \times CRF + TEC}{E_{annual}} \quad (20)$$

where E_{annual} represents the annual electricity generation, produced by the proposed model and represented by Wnet kW x 8000 h/year.

The IRR is determined as the discount rate at which the net present value equals zero. For uniform cash flow, this equation can be represented as [43]:

$$IRR = \frac{TIO}{TIC}\left(1 - \frac{1}{(1+IRR)^N}\right) \quad (21)$$

In the base-case scenario (Table 7-a), the system achieves an NPV of \$9.145 million, an IRR of 25.79%, and a PBP of 5.15 years, indicating design-point economic estimates under the assumed conditions, including prescribed thermal input and equivalent annual operating hours. The calculated LCOE is 0.1437 \$/kWh, which remains lower than the assumed electricity selling price under the adopted economic assumptions. Table 8 presents a sensitivity analysis of electricity and heat prices, revealing a strong positive correlation with economic performance. As energy prices increase, the NPV rises from \$3.16 million to \$13.55 million, and the IRR increases from 16.6% to 32.54%, while the payback period decreases from 9.68 years to 3.85 years. These findings indicate improved economic performance under favorable energy pricing assumptions.

Table 8. Sensitivity of economic indicators to electricity and heat prices at TIT = 800 °C

Case	Cost of Electricity Produced (\$/kWh)	Cost of Heat Produced (\$/kWh)	NPV (\$)	IRR (%)	PBP (years)
Low	0.17	0.08	3,162,000	16.6	9.68
Medium	0.2	0.1	6,082,000	21.08	6.75
Base	0.232	0.116	9,145,000	25.79	5.15
High	0.28	0.12	13,550,000	32.54	3.85

Further, the sensitivity analysis presented in Table 9 examines the effect of heat price on the economic performance of the proposed system while maintaining the electricity price at 0.232 \$/kWh. As the heat price increases from 0.06 to 0.14 \$/kWh, the NPV increases from \$8,605,000 to \$9,376,000, while the IRR improves from 24.96% to 26.14%. Correspondingly, the PBP decreases from 5.372 to 5.06 years. These results indicate that the economic performance of the system is positively influenced by the value assigned to the recovered low-grade heat. However, the relatively moderate variation in the economic indicators also suggests that the overall project economics remain primarily dependent on electricity revenue.

Table 9. Sensitivity of economic indicators to heat price at TIT = 800 °C and cost of electricity produced = 0.232 \$/kWh

Cost of Heat Produced(\$/kWh)	NPV(\$)	IRR(%)	PBP(years)
0.06	8,605,000	24.96	5.372
0.08	8,798,000	25.25	5.29
0.1	8,990,000	25.55	5.21
0.12	9,183,000	25.84	5.13
0.14	9,376,000	26.14	5.06

3.5 Limitations of the present study

The present study provides a steady-state, system-level thermodynamic, exergy, and economic assessment of the proposed RR sCO_2–RP ORC configuration. Several simplifying assumptions have been adopted to maintain a tractable design-point model, and their implications for practical system performance should therefore be recognized. In view of these considerations, the following limitations should be recognized:

- Pressure losses in heat exchangers, piping, and other flow passages are neglected. In a practical sCO_2 system, these pressure losses would increase the effective compression requirement and reduce the available turbine expansion work. They may also modify temperature matching within the recuperators and consequently reduce both thermal and exergy efficiencies compared with the present predictions.

Therefore, the reported performance should be regarded as an idealized design-point estimate under negligible pressure-drop conditions.

- Heat losses from the components to the surroundings are neglected. Actual primary heaters, reheaters, recuperators, piping, and other high-temperature components will experience thermal losses, which would reduce the useful heat transferred to the working fluids and increase the deviation between the predicted and practical system performance. The present model therefore represents an internally insulated power-block condition.
- The turbines, compressors, and other major components are evaluated using fixed isentropic efficiencies. Their efficiencies and operating characteristics can vary with mass flow rate, pressure ratio, rotational speed, and load. Consequently, off-design operation of the turbomachinery is not explicitly captured. Under part-load or variable-load conditions, the actual net power and cycle efficiencies may differ from the design-point values reported in this study.
- The solar subsystem is represented through prescribed thermal boundary conditions rather than a detailed optical, receiver, and solar-field model. The effect of solar availability is investigated parametrically through variations in DNI; however, transient solar-field and receiver dynamics are not explicitly resolved. Variations in optical efficiency, receiver heat losses, and solar-field operating conditions are therefore not explicitly considered. The present DNI analysis represents steady-state variations in solar availability rather than a site-specific annual solar-resource profile. Similarly, thermal energy storage and its interaction with the power block are not considered. Thus, the DNI results should be interpreted as steady-state sensitivity to prescribed solar availability rather than an annual or transient assessment of a complete CSP plant.
- Finally, the economic analysis uses an equivalent annual operating duration and prescribed energy prices. These assumptions are intended for comparative design-point assessment and do not represent a site-specific operating profile or universally applicable energy-market conditions. Actual economic performance would depend on solar-resource availability, plant capacity factor, thermal energy storage, component degradation, maintenance requirements, financing conditions, and local electricity and heat markets.

These limitations do not affect the intended purpose of the present study, which is to characterize the thermodynamic interactions, exergy distribution, heat-cascading behavior, and indicative economic performance of the proposed integrated cycle. Detailed pressure-drop modeling, heat-loss estimation, component off-design modeling, transient solar-field modeling, and annual CSP-system performance assessment are identified as important areas for future work.

4 Conclusions

An RR sCO_2 Brayton cycle integrated with RP ORC bottoming cycle is evaluated in the present study under prescribed solar input conditions. Based on the thermodynamic and economic analyses, the following conclusions are drawn:

- Thermodynamic insight: The integrated sCO_2 and ORC system effectively utilizes high-temperature heat, with reheating playing a key role in enhancing power output. Exergy analysis reveals that heat exchangers are the primary sources of irreversibility due to finite temperature differences during heat transfer. This indicates that overall system performance is predominantly limited by heat-transfer constraints rather than by turbomachinery inefficiencies.
- Parametric behavior: Integrated system performance is strongly influenced by TIT, with higher TIT leading to significant improvements in both thermal and exergy efficiencies. In contrast, increases in CIT and compressor outlet pressure reduce performance due to higher compression work and degraded recuperation effectiveness. While increasing CIP enhances the sCO_2 cycle performance, its effect on the integrated system is marginal because reduced heat availability reduces ORC performance. The SR governs the trade-off between internal heat recovery and bottoming cycle utilization, while condenser temperature significantly affects ORC performance. Variations in DNI show that useful work increases with solar input, whereas exergy efficiency peaks at moderate irradiance and declines at higher levels due to increased irreversibilities.
- Economic performance: Under the assumed design-point operating conditions, the proposed integrated system yields an NPV of \$9.145 million, an IRR of 25.79%, and a payback period of 5.15 years. The calculated LCOE is 0.1437 \$/kWh. These values represent indicative economic estimates based on simplified operating assumptions and should not be interpreted as full plant-level economic predictions. Sensitivity analysis further indicates that system profitability improves with increasing energy prices while remaining viable under moderate pricing conditions.

Future work should incorporate detailed solar field modeling, dynamic system analysis, and integration with thermal energy storage to assess realistic operating conditions and further improve system performance.

5 Acknowledgements

No external funding was received.

6 References

[1] International Energy Agency. (2024). *World energy outlook 2024*. https://www.iea.org/reports/world-energy-outlook-2024

[2] Intergovernmental Panel on Climate Change. (2023). *Climate change 2022: Mitigation of climate change: Working Group III contribution to the Sixth Assessment Report of the Intergovernmental Panel on Climate Change*. Cambridge University Press. https://doi.org/10.1017/9781009157926

[3] Panwar, N. L., Kaushik, S. C., & Kothari, S. (2011). Role of renewable energy sources in environmental protection: A review. *Renewable and Sustainable Energy Reviews, 15*(3), 1513–1524. https://doi.org/10.1016/j.rser.2010.11.037

[4] Raboaca, M. S., Badea, G., Enache, A., Filote, C., Răsoi, G., Rata, M., Lavric, A., & Felseghi, R. A. (2019). Concentrating solar power technologies. *Energies, 12*(6), Article 1048. https://doi.org/10.3390/en12061048

[5] Alexopoulos, S., & Hoffschmidt, B. (2017). Advances in solar tower technology. *Wiley Interdisciplinary Reviews: Energy and Environment, 6*(1), Article e217. https://doi.org/10.1002/wene.217

[6] Bauer, T., Pfleger, N., Laing, D., Steinmann, D., Eck, M., & Kaesche, S. (2013). High-temperature molten salts for solar power application. In F. Lantelme & H. Groult (Eds.), *Molten salts chemistry: From lab to applications* (pp. 415–438). Elsevier. https://doi.org/10.1016/B978-0-12-398538-5.00020-2

[7] Polimeni, S., Binotti, M., Moretti, L., & Manzolini, G. (2018). Comparison of sodium and KCl–$MgCl_2$ as heat transfer fluids in CSP solar towers with sCO_2 power cycles. *Solar Energy, 162*, 510–524. https://doi.org/10.1016/j.solener.2018.01.046

[8] Liu, J., He, Y., & Lei, X. (2019). Heat-transfer characteristics of liquid sodium in a solar receiver tube with a non-uniform heat flux. *Energies, 12*(8), Article 1432. https://doi.org/10.3390/en12081432

[9] Vignarooban, K., Xu, X., Arvay, A., Hsu, K. C., & Kannan, A. M. (2015). Heat transfer fluids for concentrating solar power systems: A review. *Applied Energy, 146*, 383–396. https://doi.org/10.1016/j.apenergy.2015.01.125

[10] Dostal, V. (2004). *A supercritical carbon dioxide cycle for next generation nuclear reactors* [Doctoral dissertation, Massachusetts Institute of Technology]. https://web.mit.edu/22.33/www/dostal.pdf

[11] White, M. T., Bianchi, G., Chai, L., Tassou, S. A., & Sayma, A. I. (2021). Review of supercritical CO_2 technologies and systems for power generation. *Applied Thermal Engineering, 185*, Article 116447. https://doi.org/10.1016/j.applthermaleng.2020.116447

[12] Sarkar, J. (2015). Review and future trends of supercritical CO_2 Rankine cycle for low-grade heat conversion. *Renewable and Sustainable Energy Reviews, 48*, 434–451. https://doi.org/10.1016/j.rser.2015.04.039

[13] Li, M. J., Zhu, H. H., Guo, J. Q., Wang, K., & Tao, W. Q. (2017). Development, technology, and applications of supercritical CO_2 power cycles in nuclear, solar, and other energy industries. *Applied Thermal Engineering, 126*, 255–275. https://doi.org/10.1016/j.applthermaleng.2017.07.173

[14] Liu, Y., Wang, Y., & Huang, D. (2019). Supercritical CO_2 Brayton cycle: A state-of-the-art review. *Energy, 189*, Article 115900. https://doi.org/10.1016/j.energy.2019.115900

[15] Guo, J. Q., Li, M. J., He, Y. L., Jiang, T., Ma, T., Xu, J. L., & Cao, F. (2022). A systematic review of supercritical carbon dioxide power cycles for energy industries: Technologies, key issues, and potential prospects. *Energy Conversion and Management, 258*, Article 115437. https://doi.org/10.1016/j.enconman.2022.115437

[16] Ahn, Y., Bae, S. J., Kim, M., Cho, S. K., Baik, S., Lee, J. I., & Cha, J. E. (2015). Review of supercritical CO_2 power cycle technology and current status of research and development. *Nuclear Engineering and Technology, 47*(6), 647–661. https://doi.org/10.1016/j.net.2015.06.009

[17] Wang, K., & He, Y. L. (2017). Thermodynamic analysis and optimization of a molten salt solar power tower integrated with a recompression supercritical CO_2 Brayton cycle based on integrated modeling. *Energy Conversion and Management, 135*, 336–350. https://doi.org/10.1016/j.enconman.2016.12.085

[18] Chen, J., Cheng, K., Li, X., Huai, X., & Dong, H. (2023). Thermodynamic evaluation and optimization of supercritical CO_2 Brayton cycles considering recuperator types and designs. *Journal of Cleaner Production, 414*, Article 137615. https://doi.org/10.1016/j.jclepro.2023.137615

[19] Sarkar, J., & Bhattacharyya, S. (2009). Optimization of recompression supercritical CO_2 power cycle with reheating. *Energy Conversion and Management, 50*(8), 1939–1945. https://doi.org/10.1016/j.enconman.2009.04.015

[20] Sarkar, J. (2009). Second law analysis of supercritical CO_2 recompression Brayton cycle. *Energy, 34*(9), 1172–1178. https://doi.org/10.1016/j.energy.2009.04.030

[21] Ahmad, F., Mahatab, F., Mahmud, S., & Ehsan, M. M. (2024). Comprehensive analysis of a hybrid solar-assisted supercritical CO_2 reheat recompression Brayton cycle for enhanced performance. *International Journal of Thermofluids, 24*, Article 100926. https://doi.org/10.1016/j.ijft.2024.100926

[22] Lykas, P., Georgousis, N., Bellos, E., & Tzivanidis, C. (2022). Investigation and optimization of a CO_2-based polygeneration unit for supermarkets. *Applied Energy, 311*, Article 118717. https://doi.org/10.1016/j.apenergy.2022.118717

[23] Khan, Y., Mishra, R. S., Raman, R., & Hashmi, A. W. (2023). Parametric evaluation of solar integrated combined partial cooling supercritical CO_2 cycle and Organic Rankine Cycle using low global warming potential fluids. *Journal of Thermal Engineering, 9*(5), 1140–1152. https://doi.org/10.18186/thermal.1370699

[24] Salhi, I., Sadni, F. E., Belhora, F., & Hajjaji, A. (2025). Thermodynamic analysis of basic and regenerative organic Rankine cycle configurations using six working fluids: A parametric study with CoolProp in MATLAB. *Journal of Energy Resources Technology, Part A, 1*(4), Article 042101. https://doi.org/10.1115/1.4067544

[25] Park, S. C., Son, C. H., Lee, H. S., Lim, S. T., Yoon, J. W., Choi, M. K., & Seol, S. H. (2023). Performance analysis of an organic Rankine cycle with an internal heat exchanger considering turbine pressure ratio and efficiency. *Energy, 285*, Article 129507. https://doi.org/10.1016/j.energy.2023.129507

[26] Braimakis, K., & Karellas, S. (2018). Energetic optimization of regenerative organic Rankine cycle configurations. *Energy Conversion and Management, 159*, 353–370. https://doi.org/10.1016/j.enconman.2017.12.093

[27] Georgousis, N., Lykas, P., Bellos, E., & Tzivanidis, C. (2022). Multi-objective optimization of a solar-driven polygeneration system based on CO_2 working fluid. *Energy Conversion and Management, 252*, Article 115136. https://doi.org/10.1016/j.enconman.2021.115136

[28] Liang, Y., Chen, J., Luo, X., Chen, J., Yang, Z., & Chen, Y. (2020). Simultaneous optimization of a combined supercritical CO_2 Brayton cycle and organic Rankine cycle integrated with a concentrated solar power system. *Journal of Cleaner Production, 266*, Article 121927. https://doi.org/10.1016/j.jclepro.2020.121927

[29] Ehsan, M. M., Guan, Z., & Klimenko, A. Y. (2018). A comprehensive review on heat transfer and pressure drop characteristics and correlations with supercritical CO_2 under heating and cooling applications. *Renewable and Sustainable Energy Reviews, 92*, 658–675. https://doi.org/10.1016/j.rser.2018.04.106

[30] Ehsan, M. M., Guan, Z., Gurgenci, H., & Klimenko, A. (2020). Feasibility of dry cooling in supercritical CO_2 power cycle in concentrated solar power application: Review and a case study. *Renewable and Sustainable Energy Reviews, 132*, Article 110055. https://doi.org/10.1016/j.rser.2020.110055

[31] Ehsan, M. M., Awais, M., Lee, S., Salehin, S., Guan, Z., & Gurgenci, H. (2023). Potential prospects of supercritical CO_2 power cycles for commercialisation: Applicability, research status, and advancement. *Renewable and Sustainable Energy Reviews, 172*, Article 113044. https://doi.org/10.1016/j.rser.2022.113044

[32] Ehsan, M. M., Wang, X., Guan, Z., & Klimenko, A. Y. (2018). Design and performance study of dry cooling system for 25 MW solar power plant operated with supercritical CO_2 cycle. *International Journal of Thermal Sciences, 132*, 398–410. https://doi.org/10.1016/j.ijthermalsci.2018.06.024

[33] Ehsan, M. M., Duniam, S., Li, J., Guan, Z., Gurgenci, H., & Klimenko, A. (2020). A comprehensive thermal assessment of dry cooled supercritical CO_2 power cycles. *Applied Thermal Engineering, 166*, Article 114645. https://doi.org/10.1016/j.applthermaleng.2019.114645

[34] Ehsan, M. M., Guan, Z., Klimenko, A. Y., & Wang, X. (2018). Design and comparison of direct and indirect cooling system for 25 MW solar power plant operated with supercritical CO_2 cycle. *Energy Conversion and Management, 168*, 611–628. https://doi.org/10.1016/j.enconman.2018.04.072

[35] Ehsan, M. M., Duniam, S., Guan, Z., Gurgenci, H., & Klimenko, A. (2019). Seasonal variation on the performance of the dry cooled supercritical CO_2 recompression cycle. *Energy Conversion and Management, 197*, Article 111865. https://doi.org/10.1016/j.enconman.2019.111865

[36] Ehsan, M. M., Guan, Z., Gurgenci, H., & Klimenko, A. (2020). Novel design measures for optimizing the year-long performance of a concentrating solar thermal power plant using thermal storage and a dry-cooled supercritical CO_2 power block. *Energy Conversion and Management, 216*, Article 112980. https://doi.org/10.1016/j.enconman.2020.112980

[37] Khan, T. E., Zaman, M., Ehsan, M. M., & Khan, Y. (2025). Thermal analysis of a main compression intercooling supercritical CO_2 cycle cascaded with flash tank enhanced compression–absorption refrigeration cycle. *Energy Conversion and Management: X, 25*, Article 100868. https://doi.org/10.1016/j.ecmx.2024.100868

[38] Siddiqi, M. A., & Atakan, B. (2012). Alkanes as fluids in Rankine cycles in comparison with water, benzene, and toluene. *Energy, 45*(1), 256–263. https://doi.org/10.1016/j.energy.2012.06.005

[39] Javed, S., & Tiwari, A. K. (2023). Performance assessment of different organic Rankine cycle configurations driven by solar energy. *Process Safety and Environmental Protection, 171*, 655–666. https://doi.org/10.1016/j.psep.2023.01.039

[40] Khaliq, A., Mokheimer, E. M. A., & Yaqub, M. (2019). Thermodynamic investigations on a novel solar-powered trigeneration energy system. *Energy Conversion and Management, 188*, 398–413. https://doi.org/10.1016/j.enconman.2019.03.026

[41] Mishra, S. K., Rehalia, A. S., Verma, A. K., & Yadav, L. (2024). Thermo-economic analysis of a solar-powered trigeneration system with integrated ejector-absorption recompression and modified organic Rankine cycle. *Journal of Engineering for Gas Turbines and Power, 146*(5), Article 051024. https://doi.org/10.1115/1.4064439

[42] Turchi, C. S., Ma, Z., Neises, T., & Wagner, M. (2012). Thermodynamic study of advanced supercritical carbon dioxide power cycles for high-performance concentrating solar power systems. In *Proceedings of the ASME 2012 6th International Conference on Energy Sustainability (ES2012)* (pp. 375–383). ASME. https://doi.org/10.1115/ES2012-91179

[43] Tzivanidis, C., & Bellos, E. (2019). Energetic, exergetic, and financial investigation of a biomass-driven trigeneration system. *Journal of Energy Engineering, 145*(6), Article 04019020. https://doi.org/10.1061/(ASCE)EY.1943-7897.0000622

[44] Baral, S. (2021). Thermodynamic and financial assessment of a concentrated solar power plant hybridized with a biomass-based organic Rankine cycle, thermal energy storage, hot springs and CO_2 capture system. *International Journal of Low-Carbon Technologies, 16*(2), 361–375. https://doi.org/10.1093/ijlct/ctaa069

[45] Saini, P., Singh, J., & Sarkar, J. (2021). Novel combined desalination, heating, and power system: Energy, exergy, economic, and environmental assessments. *Renewable and Sustainable Energy Reviews, 151*, Article 111612. https://doi.org/10.1016/j.rser.2021.111612

[46] Mohammadi, K., Ellingwood, K., & Powell, K. (2020). Novel hybrid solar tower–gas turbine combined power cycles using supercritical CO_2 bottoming cycles. *Applied Thermal Engineering, 178*, Article 115588. https://doi.org/10.1016/j.applthermaleng.2020.115588

[47] Shankar, A., Saxena, A. K., & Mazumdar, R. (2024). *Concentrating solar power plants with storage: Deployment essential now*. The Energy and Resources Institute. https://www.solarpaces.org/wp-content/uploads/2024/02/India-Concentrating-Solar-Power-Plants-with-Storage-Deployment-Essential-Now.pdf

7 Conflict of interest statement

There are no interest conflicts to declare

8 Author contributions

Parmod Kumar: conceptualization, methodology, literature review, formal analysis, data analysis, results generation, writing – original draft, and writing – review and editing. Shahnawaz Alam: supervision, methodology, critical review. Kamran Rasheed: supervision, review, formal analysis, writing and editing.

9 Data availability statement

The data generated and used in these findings may be requested from the corresponding author upon reasonable request.

10 Supplementary materials

There are no supplementary materials to include.

Paper submitted: 13.06.2026.

Paper accepted: 11.09.2026.

This is an open access article distributed under the CC BY 4.0 terms and conditions